Title
Design of the Superconducting Magnet System for a 45 GHz ECR Ion Source

Authors
Sabbi, GS
juchno, MJ
Ravaioli, ER
et al.

Publication Date
2017-08-10

Peer reviewed

LBNL Report 2001036
August 10, 2017

Design of the Nb_3Sn Superconducting Magnet System for the 45 GHz ECR Ion Source at IMP

G. Sabbi, R. Hafalia, M. Juchno, W. Lu, I. Pong, E. Ravaioli, D. Xie, X. Wang, LBNL

L. Sun, W. Wu, H.W. Zhao, and L. Zhu. IMP

Contents

Work Performed under Agreement No. FP00002698 between The Regents of the University of California (as the Management and Operating Contractor for the Ernest Orlando Lawrence Berkeley National Laboratory Operating Under Prime Contract No. DE-AC02-05CH11231 for the U. S. Department of Energy) and the Institute of Modern Physics of the Chinese Academy of Science.

1 Introduction

Lawrence Berkeley National Laboratory (LBNL) in collaboration with the Institute of Modern Physics (IMP) has designed the Nb_3Sn superconducting magnet system for a new fourth-generation ECR ion-source that will be part of High Intensity Heavy Ion Accelerator Facility (HIAF) in Lanzhou, China [1]. The main design parameters of the ECR source are summarized in Table I.

Parameter	Unit	Value
Microwave frequency, f_{rf}	GHz	45
Resonant heating field, B_{ECR}	T	1.6
Injection confinement field, B_{inj}	T	>6.4
Extraction confinement field, B_{extr}	T	>3.4
Radial confinement field, B_{rad}	T	>3.2
Mirror length	mm	500
Plasma chamber ID	mm	150
Warm bore ID	mm	170

Table I – ECR system parameters and magnet requirements

2 Magnetic and mechanical design

The target microwave frequency of 45 GHz is a significant step beyond the current state of the art of 28 GHz [2]. The corresponding peak field in the coil approaches 12 T - requiring the use of Nb_3Sn conductor. The coil system is based on the traditional sextupole-in-solenoid configuration

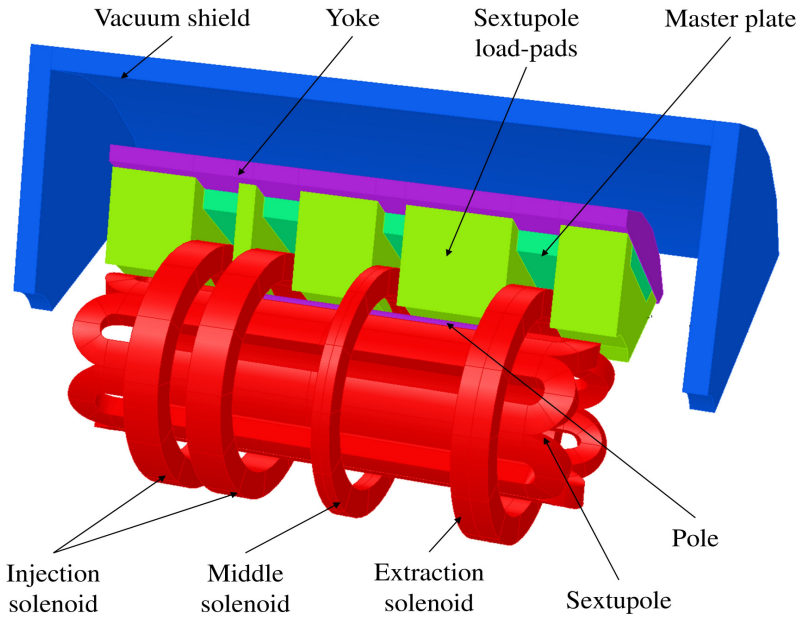

Fig. 1. Magnet cold mass

Parameter	Unit	S	M	E	I
Nominal current I_{nom}	A	654	380	626	692
Peak conductor field at I_{nom}	T	11.3	5.0	9.7	11.8
Operating temperature	K	4.2	4.2	4.2	4.2
Inner diameter	mm	200	336	336	336
Outer diameter	mm	276	430	430	430
Coil length	mm	857.4	30	60	2x60
Conductor packing factor	-	0.65	0.7	0.7	0.7

Table II: Magnet parameters

Parameter	Unit	Value
Critical current density at 4.2 K, 12 T	$kAmm^{-2}$	2.4
Wire diameter	mm	1.3
Copper/non-Copper ratio	-	0.96
RRR of the copper matrix	-	250
Filament twist pitch	mm	42
Insulation thickness	μm	65

Table III: Conductor parameters

(see Fig. 1), which allows minimizing the magnetic field in the sextupole (S) coil conductor by placing it close to the plasma chamber. The axial field confinement is provided by a solenoid system consisting of an injection (I), middle (M) and extraction (E) solenoid. This coil configuration is used in present-day superconducting ECR magnets - including VENUS at LBNL [2] and FRIB at Michigan State University [3]. However, the higher confinement field required for 45 GHz operation and the transition from Niobium-Titanium (NbTi) to Niobium-Tin (Nb_3Sn) superconductor introduce new, significant challenges, particularly in terms of the stress management of the brittle Nb_3Sn superconductor. Special tooling and fixtures are required for handling and reacting Nb_3Sn coils after winding. Also, strict limits on the maximum stress and strain need to be respected to prevent conductor degradation and the support structure has to prevent any conductor motion while minimizing the radial gap between the sextupole and solenoids.

All coils of the magnet system are wound with the same Nb_3Sn round wire. Parameters of the coil system are summarized in Table II and conductor parameters are shown in Table III. The injection solenoid is split in two modules due to mechanical considerations [2], wire piece length availability, and quench protection.

The new support structure is based on an aluminum shell surrounding the coils and iron yoke and is pre-tensioned using water-pressurized bladders and interference keys. This concept was originally developed for the LBNL high field dipole program [4]-[6] and adopted by LARP [7]. However, the application of this approach to ECR magnets requires significant modifications with respect to accelerator magnets, due to the nesting of sextupole and solenoid coils, and the complex Lorentz force configuration introduced by their combined fields and currents. In a previous design study for a 56 GHz ECR [8], a two-stage system was adopted, with the sextupole

pre-loaded by the solenoid assembly, and the solenoid assembly pre-loaded by the aluminum shell. For the 45 GHz design, we developed a new approach where the aluminum shell supports the sextupole through longitudinally segmented loading pads placed in-between solenoids (Fig. 1). These sextupole loading pads directly bear against thin curved, full-length "collar" plates that are bolted around the coils. This approach requires splitting the longer injection solenoid into two sub-coils with an axial gap, in order to reduce a long, unsupported longitudinal span between sextupole pads. Each solenoid is individually wound around a stainless steel bobbin and radially pre-loaded by tensioned aluminum banding. The solenoids longitudinally positioned and restrained by connecting them to a series of stainless steel "intercostal" elements. The aluminum shell provides the final preload through a second set of loading pads located in-between the pads of the first set. Longitudinal pre-load is applied to both sextupole and solenoid sub-assemblies by aluminum rods and end plates.

Components of the structure and their main sub-assemblies are shown in Fig. 2 and Fig. 3.

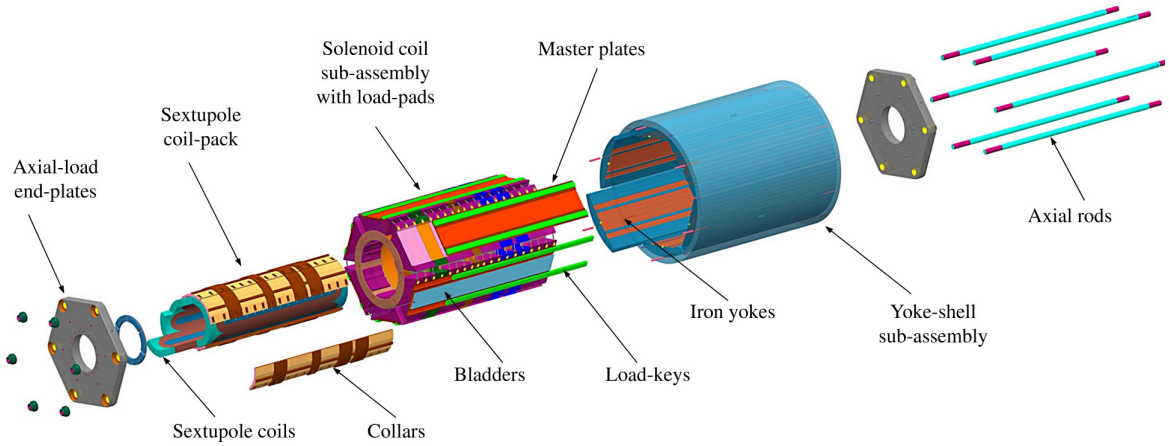

Fig. 2. Exploded view of the magnet structure.

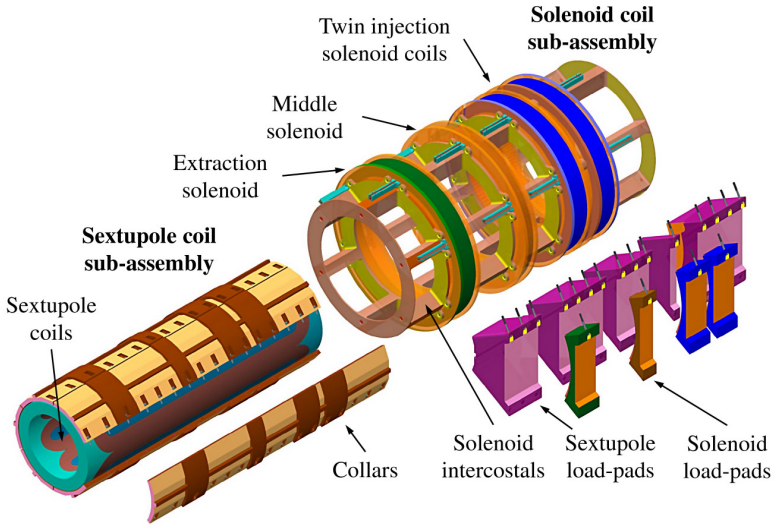

Fig. 3. Coil assembly.

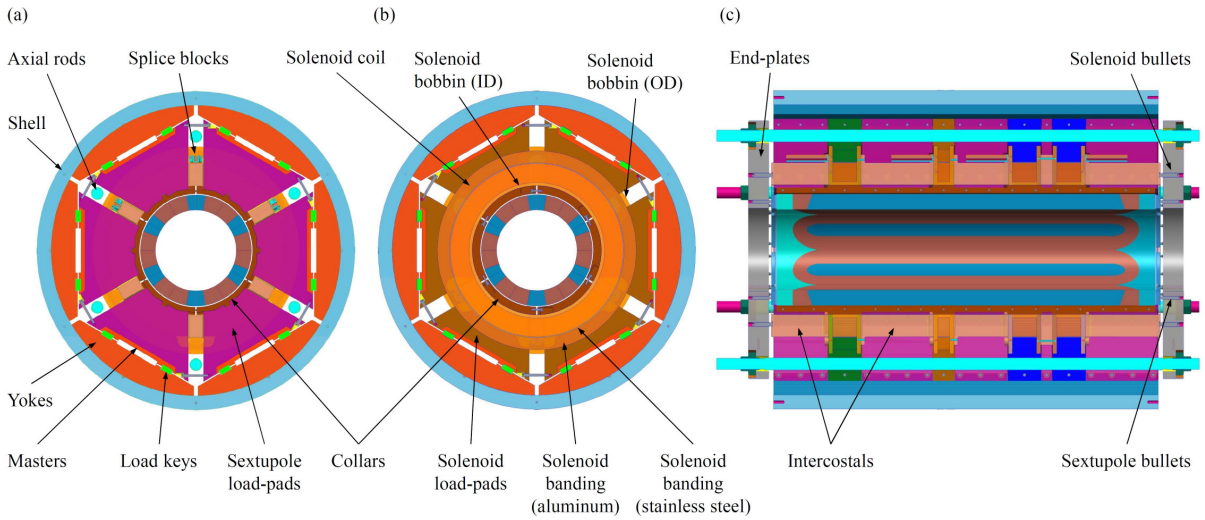

Fig. 4. Cross-section of the assembled magnet: (a) in the section of the magnet between solenoids; (b) in the section of the magnet in the middle of a solenoid coil; (c) vertical cross-section along the magnet length.

3 Magnet Components

3.1 Coil sub-assemblies

Sextupole sub-assembly: Sextupole coils are individually wound around iron poles with titanium tips. Conductor at the coil ends is held by aluminum-bronze end-shoes and the whole coil is reacted in its own heat-treat fixture and then vacuum-impregnated with an epoxy resin in a separate potting fixture. The assembly of sextupole coils is facilitated by bolting six, full-length, stainless steel collars around the coils. The collar cross-section is optimized to increases rigidity and allows for a more even distribution of the pre-load force imparted from the aluminum shell via longitudinally spaced, sextupole load-pads.

Solenoid Sub-assembly: Each solenoid coil is wound under tension on a separate stainless steel former/bobbin. Before winding, a series of laminations Mica sheets are applied to the former's conductor-contact surfaces to provide slip planes and insulation. To accommodate the necessary quench protection and detection, the solenoid is wound in two layers – with a Nb_3Sn-to-Nb_3Sn splice joint. The joint is accomplished after heat treating. Two layers of stainless steel wire are wound on top of the superconductor to protect it and control the coil dimension during reaction. After reaction and prior to vacuum impregnation, Mylar slip planes are wrapped around the outer diameter (over the stainless steel wire) and then the tensioned, aluminum-strip banding is wound around the coil. The aluminum banding provides a partial preload to the solenoid. Additional preload is applied by solenoid load-pads, which are assembled around each coil, and are coupled with the external shell structure. Solenoid coils are separated longitudinally and connected together into a sub-assembly by titanium intercostal components. The solenoid intercostal elements are designed to allow the sextupole load-pads to pass through to the coil-pack.

Support structure: The external support structure consists of a strain-gauge instrumented

aluminum cylinder and an arrangement of six iron yokes pre-assembled together into a yoke-shell sub-assembly using temporary yoke-gap keys that are removed during the final, room-temperature, magnet loading operation. The strain-gauges on the shell will be monitored during bladder and key operations at final magnet assembly. Loading keys and bladders are inserted into corresponding channels between the yokes and the iron master plates (see Fig 4). Sextupole loading pads and solenoid pads are assembled around combined sextupole coil-pack and solenoids and bolted together prior to insertion into the external support structure.

Axial pre-load system: The coils are pre-loaded axially by an array of six, full-length, aluminum axial rods that are pre-tensioned against two stainless steel end-plates pushing on sextupole coil-ends via an arrangement of push-bullets. A secondary set of push-bullets installed in the end-plates applies axial pre-load to the solenoid sub-assembly. Fig. 4c shows the cross-section of the magnet and its axial pre-load system.

3.2 Assembly and Loading

The first part of the assembly procedure requires assembling three sub-assemblies: the yoke-shell external structure, the sextupole coil-pack and the solenoid coil sub-assembly. The two coil sub-assemblies can be combined as separate units or, alternatively, the solenoids and intercostal elements can be assembled around the sextupole coil-pack. The sextupole load-pads and solenoid pads are assembled and bolted around the combined coil assemblies and the final coil-pack is inserted into the yoke-shell sub-assembly along with the master plates, bladders and initial load-keys.

During loading operations, the bladders are pressurized with water in order to open gaps between yokes and master plates to insert shimmed load-keys. This action simultaneously stretches the outer structure and compresses the load-pads and the coil assemblies. After attaining the target preload (from monitoring the shell strain-gauges) the bladders are deflated and removed. The load-keys are locked between the pre-tensioned aluminum shell and the compressed coil-pack. The axial pre-load is provided by a set of aluminum rods that are pre-tensioned during loading operation using a hydraulic piston system. The end-plates, which are drawn together by the axial rods, push on the sextupole coil-ends with a set of push-bullets. After the room temperature pre-load is set for the sextupole coils, a secondary system of bullets is adjusted to contact with exposed surfaces of the end solenoid intercostal components.

Cooling down the magnet to cryogenic temperatures increases the pre-load level due to the relatively higher thermal contraction of aluminum components with respect to the rest of the magnet structure. The shrinking aluminum shell increases the radial pre-load imparted to the sextupole coils as well as to solenoids, which also have their own aluminum strip banding. Shrinkage of aluminum rods, correspondingly, increases the pre-load on the sextupole coil-ends and also the solenoid sub-assembly to constrain axial displacement.

4 Mechanical Analysis

4.1 FEM model

Several ANSYS models were developed in support of the magnet and structure development.

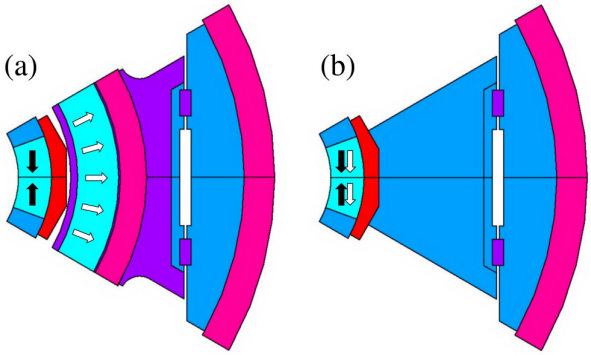

Fig. 5. Cross-sections of the magnet used in 2D mode: (a) in the center of the injection solenoid; (b) between two solenoids. Black arrows show direction of magnetic forces due to the sextupole field. White arrows show direction of magnetic forces due to solenoid field.

The main goals were to validate and optimize the conceptual design, define target pre-load levels and evaluate the coil and the structure stresses during the magnet assembly, cool-down and operation.

The initial validation of the design was performed using two-dimensional numerical models representing two critical magnet sections that were coupled within a single model: a section at the solenoid center and another between two solenoids (see Fig. 5). The highest expected magnetic forces were applied to the modeled coils including the cross-talk forces between the coils.

The initial three-dimensional model concentrated around a section of the magnet to investigate the distribution of the loads and stresses on the sextupole coil to determine the design of the collar plates and spacing of the load-pad segments. The model evolved into a full-length model that included all main structural components of the magnet which allowed the application of the pre-loads to the coupled coil systems.

4.2 Magnetic forces

Magnetic forces acting on the coil system were calculated using a 3D finite-element magnetic model created in OPERA 3D software and transferred to the mechanical model for the stress calculation during excitation.

Due to the sextupole-in-solenoids configuration of the coil system, the sextupole coils were affected by the radial component of the solenoids' fringe field. This introduced a local variation of the magnetic force acting on the sextupole cross-section along the straight section. While in a cross-section of the coil that was not affected by the radial fringe field component of the solenoid coil (see Fig. 5a), the integrated vertical force is zero. In the case where the radial fringe field component is present (see Fig. 5b), the local integrated vertical force reaches approximately 2.5 MN/m.

The sextupole coil-ends were also affected by the fringe fields of the injection and the extraction solenoids. As the neighboring sextupole coils had opposing current polarities, they

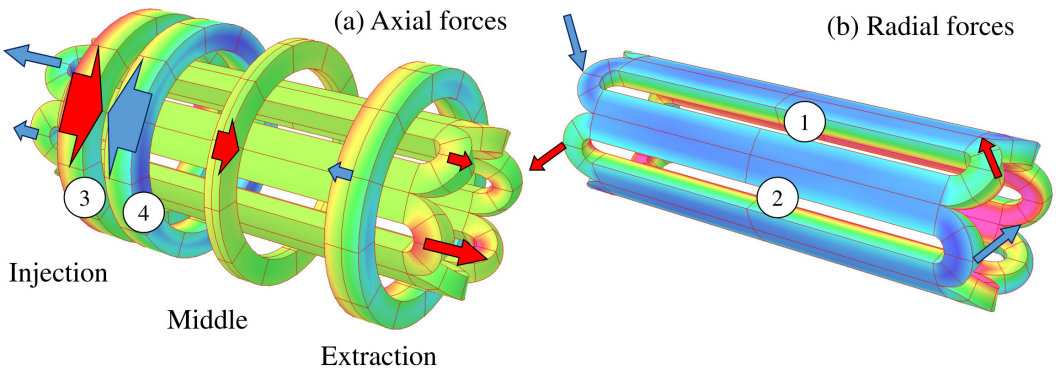

Fig. 6. Direction of (a) axial forces acting on the sextupole and the solenoid coils and direction of (b) radial forces acting on ends of the sextupole coils.

showed different magnetic force magnitudes and directions in their coil-ends as well as in the opposing ends of the same coil (see Fig. 6).

The magnetic forces acting on solenoid coils were due to magnetic field generated by the coils themselves and the fields of the adjacent sextupole coils. Contributions of the sextupole coils were local and canceled out when the force was integrated across a solenoid coil. This was due to opposing current polarities in the neighboring sextupole coils. Due to longitudinal gap between the split, injection solenoid, a high attracting magnetic force acted upon the split pair of coils and it was intercepted by the intercostal structure the separated the pair. Values of the integrated magnetic forces acting on each coil are summarized in Table IV. The integrated radial (Fr), azimuthal (FΘ) and axial (Fz) components of the forces acting on the coil system components are given. For solenoid coils, axial and radial components of the forces are also expressed as an equivalent axial (Pz) and radial (Pr) magnetic pressure acting on the external axial surface and inner radius surface of each solenoid coil, correspondingly.

Parameter	F_r [kN]	F_Θ [kN]	F_z [kN]	P_z [MPa]	P_r [MPa]
Sextupole 1 end (E)	99.7	-	49.4	-	-
Sextupole 2 end (E)	-121.7	-	165.8	-	-
Sextupole 1 straight	421	-1057	-	-	-
Sextupole 2 straight	406	994	-	-	-
Sextupole 1 end (I)	-105.9	-	-166.2	-	-
Sextupole 2 end (I)	88.4	-	-55.3	-	-
Injection (3)	-	-	1749	30.9	82.4
Injection (4)	-	-	-1994	35.3	82.4
Middle	-	-	165.6	2.9	12
Extraction	-	-	-8.6	0.15	61.1

Table IV: Magnetic forces

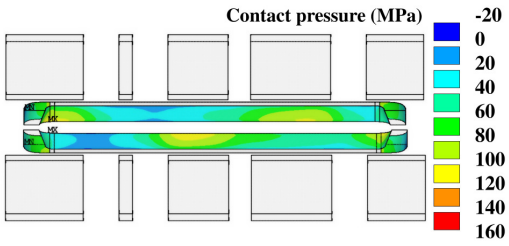

Fig. 7. Contact pressure at the interface between the sextupole coils and its pole/end-shoe. Positive values show compression. Sextupole load-pads, which transfer pre-load to the sextupole coils, are shown in gray.

4.3 Coil and structure condition

Results of the 2D analysis showed that the proposed concept of the support structure is capable of sufficiently preloading the sextupole coil. During the bladder operations and when keys were inserted at the room temperature, the maximum stress in the coil was approximately 55–75 MPa. After the cool-down, the model showed a maximum stress of approximately 143 MPa in the inner radius/pole corner areas. Due to the contribution of the solenoid coil fringe field in the magnet section between two solenoid coils, the stress distribution during the excitation was unsymmetrical and the peak stress of 129 MPa was located in the neighborhood of three poles of the magnet - in the high field zone. The azimuthal stress in the region of the other three poles was reduced but coils were under compression and they did not separate from their poles.

Pre-load from the external structure was provided to the sextupole coil-pack though the sextupole load-pads that were located between solenoid coils. These segments were situated where the strongest influence of the solenoid coil fringe field. The locally thickened collars bridged the pre-load to the segments of the sextupole coil that are underneath the solenoids. Fig. 7 shows the compression of the coil against the pole and the end-shoe after optimizing the collars' cross-sections over an unsupported span between load-pads of 80 mm. The pre-load distributed by the collars was sufficiently uniform and the sextupole coil did not separate from the pole. Fig. 8 shows the distribution of Von Mises stress in the sextupole coil. While the

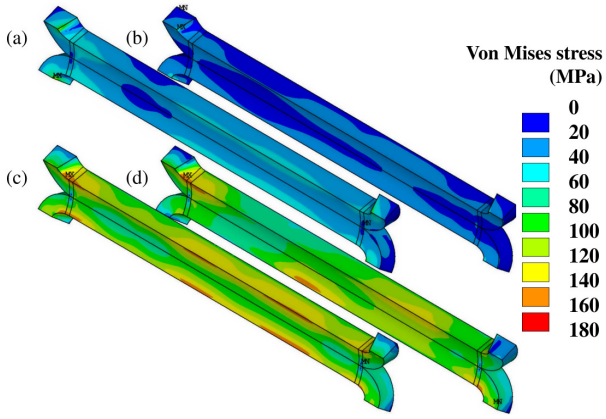

Fig. 8. Von Mises stress in the sextupole during (a) the bladder operation, (b) the room temperature pre-load, (c) cool-down and (d) excitation.

calculated stress during bladder operations with all six bladders was approximately 116 MPa, past experience showed that when using one or two bladders at the same time, the stress value drops to a similar value as with inserted load-keys, which was 67 MPa [10]. The stresses after cool-down and with magnetic forces were below 155 MPa and the peak was located at the coil-ends.

The radial pre-load was applied to the solenoid coils using a 30 mm thick layer of pre-tensioned aluminum strip-banding compressed by the stainless steel solenoid loading pads and the external support structure. The maximum stress in solenoid coils was 100 MPa after cool-down and 126 MPa when magnetic forces were applied. Results of the analysis showed that, when magnetic forces were applied, coils remain radially compressed and most of their inner radius surface is in contact with their formers.

5 Quench protection

Quench protection of the proposed 45 GHz design is considerably more challenging than in previous Niobium-Titanium (NbTi) ECR magnets [12]. First, the higher energy density stored in the conductor due to the higher magnetic field increases the potential for damage. Second, the normal-zone propagation velocities in the low-field regions are reduced due to higher thermal margin to quench. Third, the stabilizer fraction in Nb_3Sn internal tin wire is limited to lower range than NbTi wire, which increases the stabilizer current density. These challenges have been successfully addressed for Nb_3Sn accelerator magnets. However, accelerators magnets can benefit from high current, multi-strand cables to decrease the inductance. In the case of ECR magnets, a low current design based on a single wire is strongly preferred for compatibility with the cryogenic and current supply system. This significantly increases the magnets' self-inductances and decreases the turn-to-turn normal-zone propagation speed.

The protection of each magnet in the ECR system is analyzed separately maintaining common requirements in terms of maximum allowed hot-spot temperature Thot [K] and voltage to ground U_g [V]. The maximum values of T_{hot} and U_g are set to 350 K [13] and 1 kV. The baseline quench protection system is based on energy-extraction (EE) for each of the four independent powering circuits. An alternative system based on CLIQ [14]-[15] is also investigated for the sextupole magnet protection and will be required in order to meet the design goals without further splitting of the powering circuit. The analysis is performed with the LEDET (Lumped-Element Dynamic Electro-Thermal) program [16]-[18], which includes non-linear effects such as inter-filament coupling loss, quench-back, and reduction of the differential inductance due to coupling currents.

5.1 Protection based on energy extraction

It can be easily shown that self-protection is not a viable option for any of the four magnets. Even in the case of the shortest M solenoid, T_{hot} reaches around 400 K, which is higher than the 350 K limit. The other magnets will reach much higher temperatures leading to extensive damage. Thus, an active system is required, which detects the quench, switches off the power supply, and quickly discharges the magnet transport current I_m [A]. The baseline powering and quench protection strategy features an independent power supply and energy-extraction system

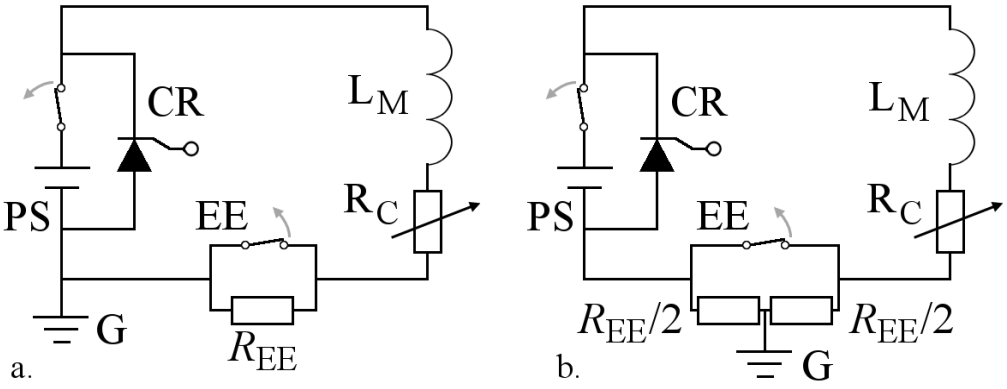

Fig. 9. Simplified electrical schematic of one of the four magnet circuits, including a power supply (PS), its crowbar (CR), the magnet (LM), its resistance developing during a quench (RC), an energy-extraction system (EE), and grounding (G). a. Standard grounding. b. Symmetric grounding.

for each of the four magnets. The simplified electrical schematic of one of the four circuits is shown in Fig. 9a. Upon quench detection, the energy-extraction switch is opened and the current is discharged due to the energy-extraction resistance R_{EE} [Ω] and coil resistance R_C [Ω]. R_{EE} is selected for each magnet as a compromise between a quick current discharge, calling for high resistance, and a low voltage to ground, calling for low resistance.

The peak voltage across the EE resistor, reached just after EE triggering, is $U_{EE}=R_{EE}I_0$, where I_0 [A] indicates the magnet current at the beginning of the discharge. This is the peak voltage to ground reached in the circuit during the quench transient, $Ug=U_{EE}$. However, it is possible to halve Ug by symmetrically grounding the circuit at the middle point of the EE resistor, as shown in Fig. 9b, hence obtaining $U_g \sim$ UEE/2.Based on the experience with similar superconductors working at similar magnetic fields and current densities, it is assumed that quench detection and validation is performed in 15 ms. The energy-extraction switching mechanism includes a silicon controlled rectifier (SCR), opening in 2 ms, and a mechanical switch, opening in 32 ms, connected in series for redundancy. Thus, the EE triggering time is 2 ms in absence of failures and 32 ms in the case of SCR failure.

The protection of each magnet is analyzed separately, neglecting the magnetic coupling between them. This approach is well justified by taking into account that the mutual inductances between magnets are much lower than their self-inductances, as shown in Table V.

	S	M	E	I
S	2.40	0.00	0.00	0.00
M	0.00	0.35	-0.08	-0.16
E	0.00	-0.08	1.27	0.08
I	0.00	-0.16	0.08	3.46

Table V: Magnet self and mutual inductances [H]

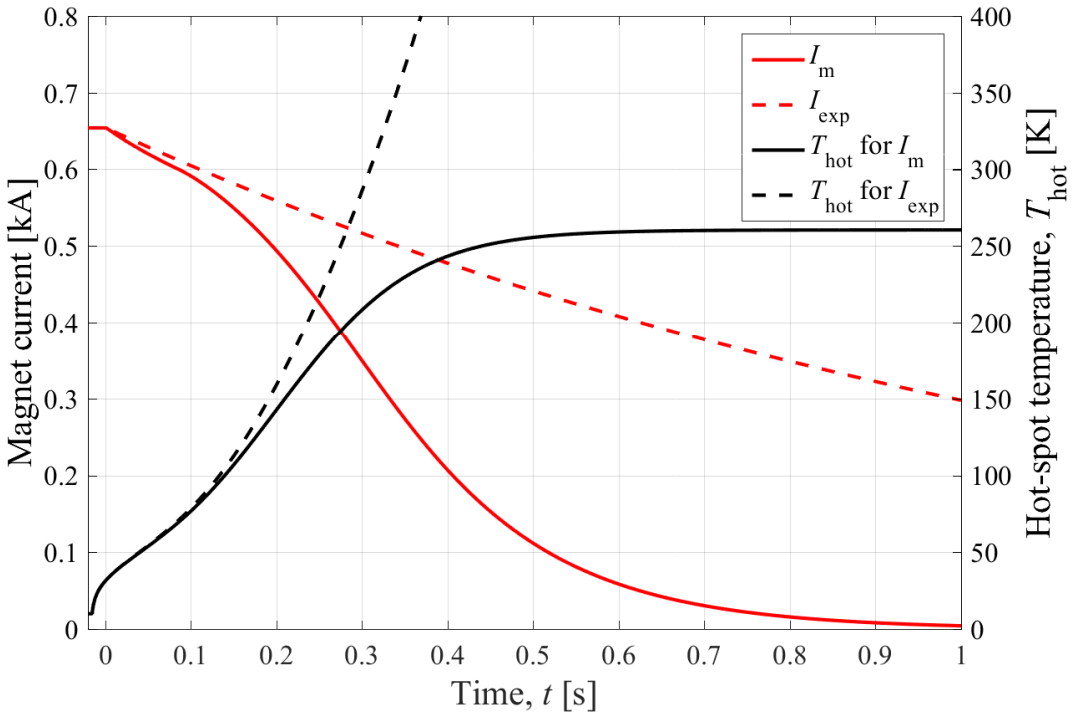

Fig. 10. Energy-extraction discharge of the sextupole magnet. Simulated current Im and hot-spot temperature T_{hot} versus time after a quench at nominal current protected by a 2 Ω energy-extraction system. The current I_{exp} calculated for a purely exponential decay and the resulting T_{hot} are also provided.

Effect of Coupling Currents on Energy-Extraction Discharge

In the absence of non-linear effects, after triggering the energy-extraction system the magnet current decay is purely exponential and follows $I_m(t)=I_{exp}(t)=I_0 \exp(-tR_{EE}/L_M)$, with L_M [H] the magnet self-inductance. However, the presence of inter-filament coupling currents significantly influences the electro-magnetic and thermal transient [17]. First, the magnet differential inductance is reduced due to the coupling currents generated in the wires. Second, the heat deposited as inter-filament coupling loss increases the local wire temperature and can cause a transition to the normal state of significant parts of the coil, hence increasing the coil resistance. As an example, the simulated current after a quench in the sextupole magnet's highest-field turn at the nominal current I_{nom} = 654 A (t = -15 ms) and subsequent triggering of a 2 Ω EE system (t = 2 ms) is shown in Fig. 10. The magnet current decay is significantly faster than a purely exponential decay. In the presented case, I_m and I_{exp} differ by 10% at t = 193 ms, and by 50% at t= 380 ms. This change occurs when large parts of the coil are transferred to the normal state due to inter-filament coupling loss, which reaches a peak power deposition of a few $mWmm^{-3}$. The time at which each wire is transferred to the normal state is plotted in Fig. 11a.

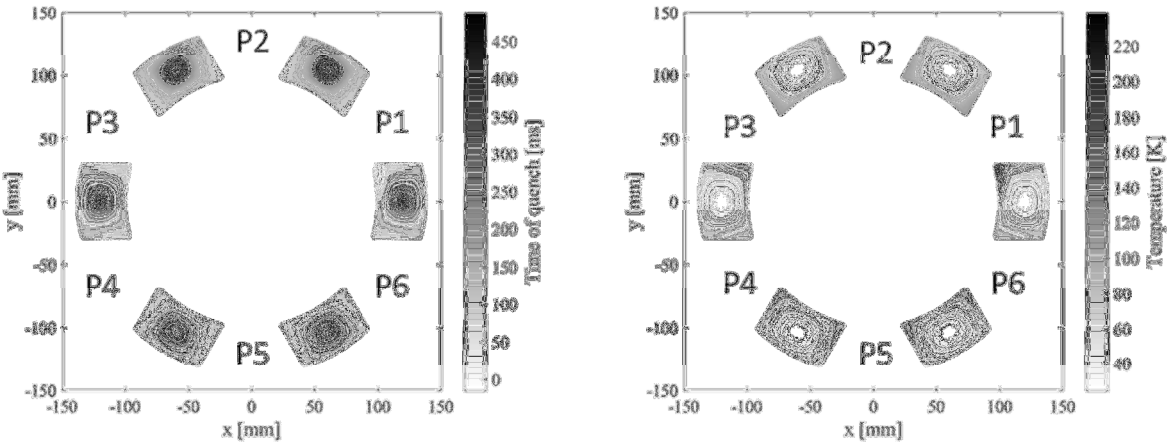

Fig. 11. Energy-extraction discharge of the sextupole magnet (I_0=654 A, R_{EE}=2). Quench starts at t = -15 ms in the highest-field wire of pole P1 and EE is triggered at t = 2 ms. (a) Simulated time at which each wire is transferred to the normal state. (b) Simulated temperature profile in the cross-section of the magnet at the end of the discharge.

About 19%, 62% and 80% of the wire volume is quenched after 100, 150, and 200 ms from EE triggering, respectively. The simulated temperature profile at the end of the discharge is shown in Fig. 11b. The bulk temperature remains between 25 and 100 K, but it reaches about 240 K in the turn where the quench started. The hot-spot temperature calculated under the more conservative assumption of adiabatic condition, plotted in Fig. 10, reaches about 260 K, well below the maximum allowed temperature of 350 K. If inter-filament coupling currents are neglected, T_{hot} increases well above 400 K, as shown in Fig. 10. This result indicates that quench-back is determinant for this magnet's quench protection with energy extraction.

Energy extraction system optimization

Current discharges are simulated for each magnet circuit at its respective I_{nom} for varying EE resistances. For each circuit, the optimum value of R_{EE}, which maintains T_{hot} below 350 K with sufficient margin while minimizing U_g, is determined. The R_{EE} values selected for the four circuits and the resulting U_g and $T_{ho}t$, in nominal and SCR failure cases, are reported in Table IV. The protection of the M and E solenoids can be achieved with R_{EE} values of 0.5 and 1.5, respectively. With this choice, even in the case of SCR failure Thot is maintained safely below

Parameter	Unit	S	M	E	I
Energy extraction resistance (R_{EE})	Ω	2.0	0.5	1.5	4.3
Peak voltage to ground (U_g)	V	654	95	470	1488
Hot spot temperature (T_{hot}) in nominal case	K	260	64	249	315
Hot spot temperature (extraction failure)	K	337	70	318	410

Table V: Energy extraction system performance assuming symmetric grounding. In the absence of symmetric grounding, all U_g values will double.

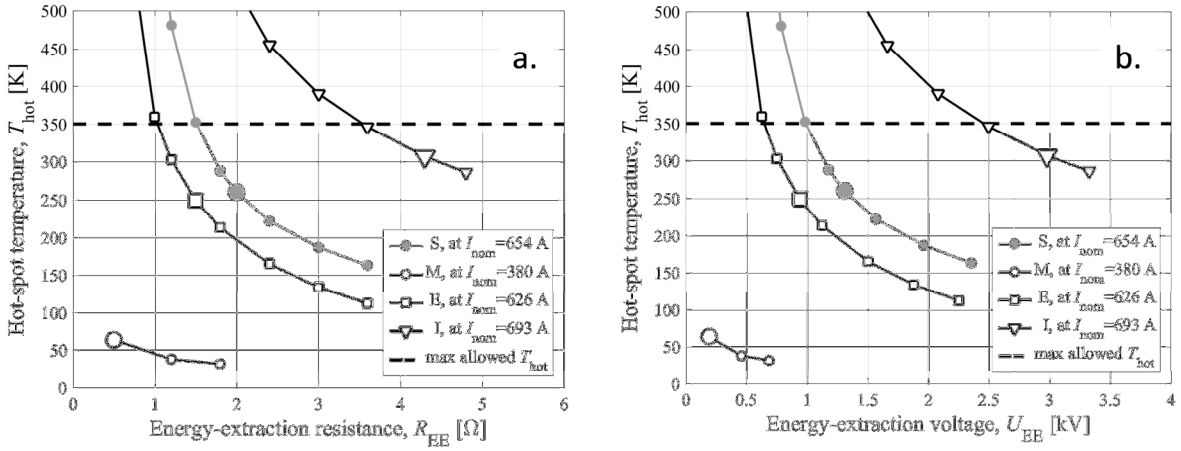

Fig. 12. Energy-extraction discharge of the four magnets. Simulated hot-spot temperature after a quench at nominal current. a. As a function of the energy-extraction resistance. b. As a function of the peak voltage across the energy-extraction resistor. Larger markers indicate design values shown in Table IV.

the 350 K temperature limit. Besides, U_g remains below 1 kV even in the case of non-symmetric grounding.

The protection of the two I solenoids in series can be attained with a 4.3 Ω EE system. However, the target 1 kV limit on U_g is overcome by a factor 1.5 and 3 in the case of symmetric or non-symmetric grounding, respectively. Furthermore, in the case of SCR failure, the 350 K limit on T_{hot} is exceeded. A possible solution to mitigate these problems is the powering of the two I solenoids in separate circuits. This option results in halving the peak voltage to ground, but at the cost of doubling the power supplies, energy-extraction systems, and current leads required for the I solenoids. In addition, the redundancy of the EE system could be improved, for example including several SCRs in series instead than one SCR in series to a slower mechanical switch.

The quench protection of the sextupole magnet can be achieved with a 2 Ω EE system. However, in the case of SCR failure T_{hot} = 337 K, close to the maximum allowed temperature. Given the uncertainties on the model assumptions, wire parameters, and material properties, this margin is unsatisfactory. Furthermore, if symmetric grounding cannot be implemented, the 1 kV limit on U_g is also exceeded. Therefore, protection of the sextupole magnet with energy-extraction is marginal.

In order to assess possible alternative choices relative to the baseline parameters of Table V, The calculated hot-spot temperatures as a function of R_{EE} and U_{EE} are plotted in Fig. 12a and Fig. 12b respectively.

5.2 Sextupole protection based on CLIQ

Powering and protecting separately sections of the sextupole magnet is a viable option. However, an alternative approach to quench protection based on the Coupled Loss Induced Quench (CLIQ) system can improve the system redundancy and reduce the peak voltages to ground without the need of doubling the powering and energy-extraction circuits. CLIQ relies on

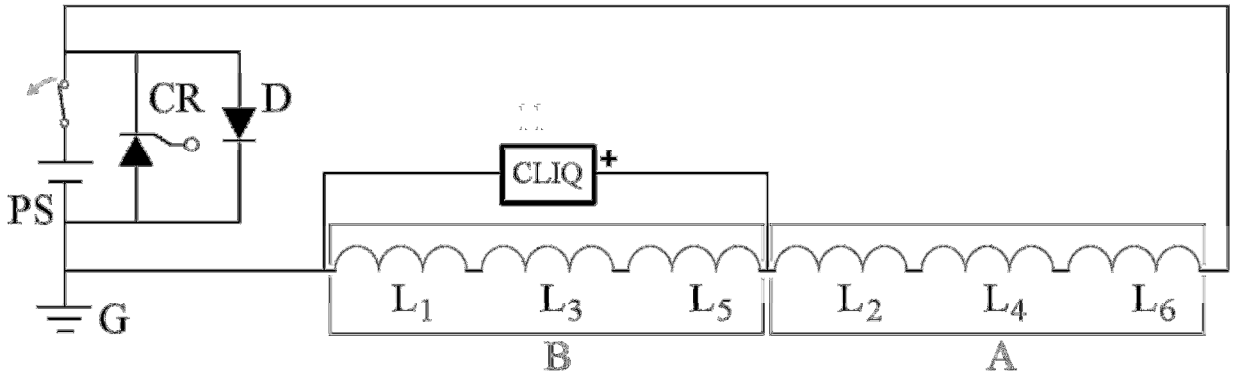

Fig. 13. Simplified electrical schematic of the sextupole circuit with CLIQ-based quench protection. L1-L6 are the six poles, numbered counter-clockwise, as shown in Fig. 4.

a capacitive discharge that introduces fast current changes in the coil sections [14]–[16]. The resulting fast changes of the local magnetic field introduce high inter-filament coupling loss [19]-[20], which in turn causes the heating of the conductor and a transition to the normal state of voluminous coil parts. This technology was successfully applied for the protection of multi-pole magnets [16], [21]–[23] and solenoids [24]. In order to maximize the effectiveness of a CLIQ system, opposite current changes should be introduced into physically adjacent coil sections [25]. Applying this criterion to the sextupole geometry, an optimized system is obtained by selecting the pole electrical order and CLIQ terminal positioning shown in Fig. 13. This configuration only requires one CLIQ terminal connected to the coil's middle point. As an example, the transient following a quench at nominal current in the S magnet and the subsequent protection using a 200 V, 80 mF CLIQ unit is presented in Fig. 14. The current I_C introduced by CLIQ is roughly equally distributed between the two coil sections A and B (see Fig. 13). As a result, the currents in the coil sections I_A and I_B oscillate, as shown in Fig. 14. The coupling loss due to the

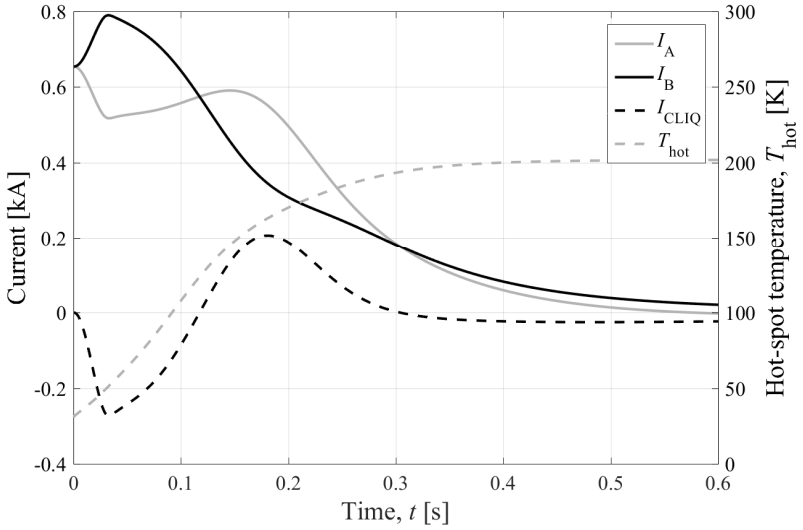

Fig. 14. Discharge of the sextupole magnet with a 200 V, 80 mF CLIQ unit. Simulated currents in the coil sections I_A and I_B, current introduced by CLIQ I_C, and hot-spot temperature T_{hot} after a quench at nominal current, versus time.

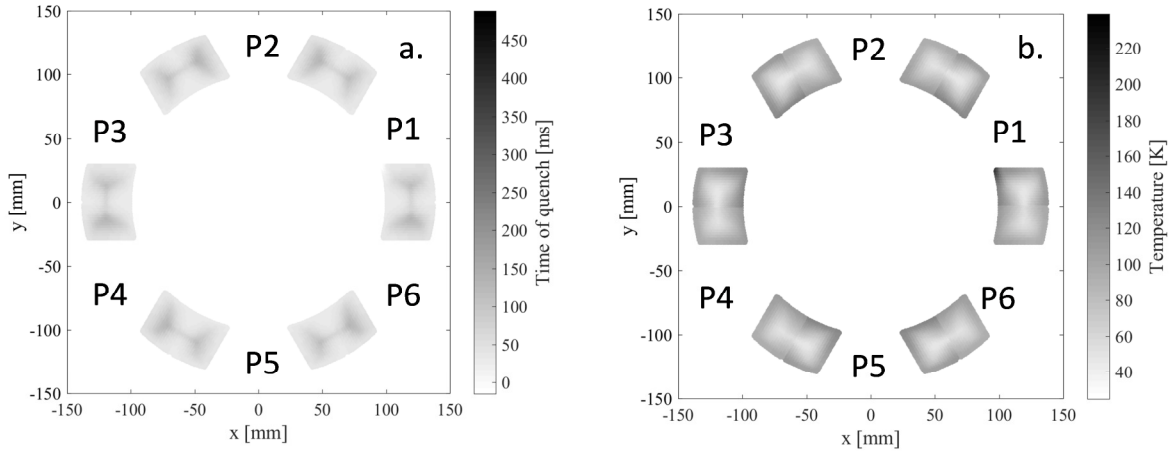

Fig. 15 Discharge of the sextupole magnet with a 200 V, 80 mF CLIQ unit (I_0=654 A). Quench starts at t = -15 ms in the highest-field wire of pole P1 and EE is triggered at t=2 ms. a. Simulated time at which each wire is transferred to the normal state. b. Simulated temperature profile in the cross-section of the magnet at the end of the discharge. The scales used in these plots are the same as those used in Fig. 11.

consequent magnetic-field change in the wires reaches a peak of about 28 mWmm^{-3}. The fast transition to the normal state induced by this local heating causes the coil resistance to rise rapidly, hence quickly discharging the magnet current. The calculated adiabatic hot-spot temperature, also plotted in Fig. 14, is 202 K, lower than that obtained using the baseline 2 Ω EE system.

The speed of the transition to the normal state can be observed in Fig. 15a. About 52% of the coil volume is quenched 50 ms after triggering CLIQ, and 92% at 50 ms. As a result, the temperature distribution in the magnet cross-section is rather homogeneous, as shown in Fig. 15b. The temperature reaches 45 to 135 K in the bulk of the magnet, and 190 K in the turn where the quench started. Similar discharges for varying values of capacitance and charging voltage of the CLIQ unit are simulated. The calculated hot-spot temperatures are plotted in Fig. 16 as a function of the peak voltage to ground during the transient. With a 40 or 80 mF CLIQ unit charged to voltages in the range 200 to 300 V it is possible to maintain T_{hot} around 200 K and U_g below 500 V. The transient shown in Fig. 14 is obtained with optimum 200 V, 80 mF CLIQ parameters, which achieve U_g = 360 V. In comparison, to keep T_{hot} below 200 K using an EE system U_g reaches values 2.5 or 5 times higher with standard or symmetric grounding, respectively, as can be observed in Fig. 16.

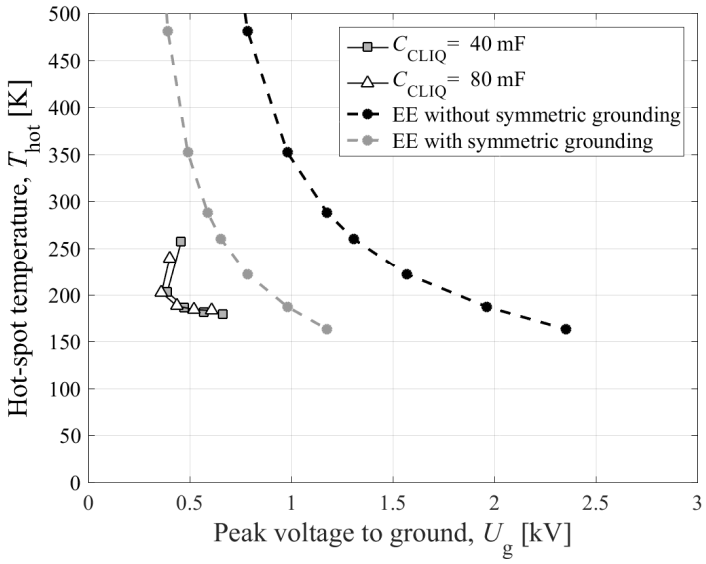

Fig. 16 Simulated hot-spot temperature after a quench at nominal current in the sextupole magnet as a function of the peak voltage to ground, for CLIQ units of capacitance 40 and 80 mF and charging voltage U0 in the range 150 to 500 V. Comparison with Thot and Ug obtained by using an EE system.

6 References

1. H.W. Zhao *et al.*, “A 45 GHz Superconducting ECR Ion Source FECRAL and Its Technical Challenges,” in Abstracts of 16th International Conference on Ion Sources, ThuPS26, 2015.
2. D. Leitner *et al.*, "Status report and recent developments with VENUS," in Proc. ECRIS, Chicago, IL, USA, 2008.
3. H. Felice *et al.*, "Design of a superconducting 28 GHz ion source magnet for FRIB using a shell-based support structure," presented at the Appl. Supercond. Conf., Charlottle, NC, USA, Aug. 10–15, 2014.
4. S. Caspi *et al.*, "The use of pressurized bladders for stress control of Superconducting Magnets," IEEE Trans. Appl. Supercond., vol. 11, no. 1, pp. 2272–2275, 2001.
5. P. Ferracin *et al.*, “Mechanical design of HD2, a 15 T Nb_3Sn dipole magnet with a 35 mm bore,” IEEE Trans. Appl. Supercond., vol. 16, no. 2, pp. 378–381, Jun. 2006.
6. D. W. Cheng *et al.*, “Design and fabrication experience with Nb_3Sn block-Type coils for high field accelerator dipoles,” IEEE Trans. Appl. Supercond, vol. 23, Jun. 2013.
7. P. Ferracin *et al.*, “Magnet Design of the 150 mm Aperture Low-β Quadrupoles for the High Luminosity LHC,” IEEE Trans. Appl. Supercond., vol. 24, no. 3, Jun. 2014.
8. S. Prestemon *et al.*, "Design of a Nb_3Sn Magnet for a 4th Generation ECR Ion Source," IEEE Trans. Appl. Supercond., vol. 19, June, 2009.

9. G. Sabbi, A. Hafalia, M. Juchno, W. Lu, E. Ravaioli, L. Sun and D. Xie, "Design of the Superconducting Magnet System for a 45 GHz ECR Ion Source", LBNL Report 2001036, August 10, 2017.
10. M. Juchno *et al.*, "Mechanical qualification of the support structure for MQXF, the Nb_3Sn low-β quadrupole for the high luminosity LHC," IEEE Trans. Appl. Supercond.
11. E. Ravaioli *et al.*, "Quench Protection of a Nb_3Sn Superconducting Magnet System for a 45 GHz ECR Ion Source," IEEE Transactions on Applied Superconductivity, to be published.
12. C. Taylor, S. Caspi, M. Leitner, S. Lundgren, C. Lyneis, D. Wutte, S. T. Wang, and J. Y. Chen, "Magnet system for an ecr ion source," IEEE Trans. Appl. Supercond., vol. 10, no. 1, pp. 224–227, March 2000.
13. G. Ambrosio, "Maximum allowable temperature during quench in Nb3Sn accelerator magnets," in Proceedings, WAMSDO 2013 Workshop on Accelerator Magnet, Superconductor, Design and Optimization: CERN Geneva, Switzerland, 15-16 Jan 2013, 2013, pp. 43–46. https://inspirehep.net/record/1277941/files/arXiv:1401.3955.pdf
14. E. Ravaioli, "CLIQ," Ph.D. dissertation, Enschede, 2015, presented on 19 June 2015. http://doc.utwente.nl/96069/
15. V. Datskov, G. Kirby, and E. Ravaioli, "AC-current induced quench protection system," Patent EP13 174 323.9, June 28, 2013.
16. E. Ravaioli, V. I. Datskov, C. Giloux, G. Kirby, H. H. J. ten Kate, and A. P. Verweij, "New, Coupling Loss Induced, Quench protection system for superconducting accelerator magnets," IEEE Transactions on Applied Superconductivity, vol. 24, no. 3, pp. 1–5, June 2014.
17. E. Ravaioli, B. Auchmann, M. Maciejewski, H. ten Kate, and A. Verweij, "Lumped-element dynamic electro-thermal model of a superconducting magnet," Cryogenics, 2016. http://www.sciencedirect.com/science/article/pii/S0011227516300832
18. E. Ravaioli, B. Auchmann, G. Chlachidze, M. Maciejewski, G. Sabbi, S. E. Stoynev, and A. Verweij, "Modeling of inter-filament coupling currents and their effect on magnet quench protection," IEEE Transactions on Applied Superconductivity, vol. 27, no. 4, pp. 1–8, June 2017.
19. A. P. Verweij, "Electrodynamics of superconducting cables in accelerator magnets," Ph.D. dissertation, Twente Univ., 15 Sep 1995.
20. M. Wilson, Superconducting Magnets, ser. Monographs on Cryogenics. Clarendon Press, 1983.
21. E. Ravaioli, H. Bajas, V. I. Datskov, V. Desbiolles, J. Feuvrier, G. Kirby, M. Maciejewski, G. Sabbi, H. H. J. ten Kate, and A. P. Verweij, "Protecting a full-scale Nb3Sn magnet with CLIQ, the new Coupling-Loss-Induced Quench system," IEEE Transactions on Applied Superconductivity, vol. 25, no. 3, pp. 1–5, June 2015.
22. E. Ravaioli, H. Bajas, V. I. Datskov, V. Desbiolles, J. Feuvrier, G. Kirby, M. Maciejewski, H. H. J. ten Kate, A. P. Verweij, and G. Willering, "First implementation of the CLIQ quench protection system on a full-scale accelerator quadrupole magnet," IEEE Transactions on Applied Superconductivity, vol. 26, no. 3, pp. 1–5, April 2016.
23. E. Ravaioli, V. I. Datskov, G. Dib, A. M. Fernandez Navarro, G. Kirby, M. Maciejewski, H. H. J. ten Kate, A. P. Verweij, and G. Willering, "First implementation of the CLIQ quench protection system on a 14-m-long full-scale LHC dipole magnet," IEEE Transactions on Applied Superconductivity, vol. 26, no. 4, pp. 1–5, June 2016.

24. E. Ravaioli, V. Datskov, A. Dudarev, G. Kirby, K. Sperin, H. ten Kate, and A. Verweij, “First experience with the new Coupling Loss Induced Quench system,” Cryogenics, vol. 60, pp. 33–43, 2014. http://www.sciencedirect.com/science/article/pii/S0011227514000162
25. E. Ravaioli, V. I. Datskov, V. Desbiolles, J. Feuvrier, G. Kirby, M. Maciejewski, K. A. Sperin, H. H. ten Kate, A. P. Verweij, and G. Willering, “Towards an optimized Coupling-loss Induced Quench protection system (CLIQ) for quadrupole magnets,” Physics Procedia, vol. 67, pp. 215–220, 2015.